J. Fluid Mech. (2018), *vol.* 840, *pp.* 106–130. © Cambridge University Press 2018
doi:10.1017/jfm.2018.14

Self-similar kinematics among efficient slender swimmers

A. J. Wiens[1,†] **and A. E. Hosoi**[1]

[1]Department of Mechanical Engineering, Massachusetts Institute of Technology, Cambridge, MA 02143, USA

(Received 16 June 2017; revised 27 November 2017; accepted 20 December 2017; first published online 7 February 2018)

We present an analysis of efficient undulatory propulsion for slender animals swimming at high Reynolds number. Using Lighthill's large-amplitude elongated-body theory, we show that optimally efficient swimming kinematics can be characterized through a single dimensionless variable ψ. This variable, ψ, is defined by a simple function of a swimming animal's body wave properties. Physically, ψ characterizes how the velocity of an animal's tail varies throughout its swimming stroke. Lighthill's model predicts that swimming efficiency is near optimal in the range $0.3 < \psi < 1.0$ and peaks at $\psi = 0.87$. At this point, the average magnitude of the tail velocity is minimized and swimming kinematics are tuned such that the thrust coefficient is as close to constant as possible throughout the swimming stroke. We use a compiled dataset of over 250 unique measurements to show that species across a wide range of size and shape fall within the optimal region.

Key words: biological fluid dynamics, propulsion, swimming/flying

1. Introduction

Biologists and engineers alike have long been captivated by the grace and fluidity of fish and other undulatory swimmers. These animals achieve locomotion by generating a backwards propagating wave along their body which interacts with the surrounding fluid to generate a propulsive force. Over the past century the relationships between body wave kinematics, animal physiology, and propulsive performance have been studied from a wide variety of perspectives, ranging from neurology and muscle dynamics to systems control and fluid mechanics. Throughout these fields, particular interest has been devoted to the problem of optimally efficient locomotion. From a biological perspective, efficiency is potentially a strong motivator of behaviour and physiology. From an engineering perspective, it is hoped that the endurance of natural swimmers can be emulated in the design of aquatic vehicles. Within the following study we explore the physics of efficient undulatory propulsion for slender animals swimming at high Reynolds number, $Re = V\ell/\nu$, where V is swimming velocity, ℓ is body length, and ν is the kinematic viscosity of the surrounding fluid.

We begin with a brief review of high-Re swimming, from the works of Lighthill up to the present day. While earlier studies such as those of Gray (1936) and

†Email address for correspondence: wiens@mit.edu

https://doi.org/10.1017/jfm.2018.14 Published online by Cambridge University Press

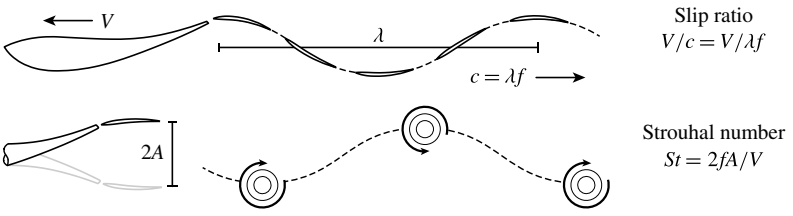


FIGURE 1. Definitions of the slip ratio and Strouhal number for undulatory swimming.

Taylor (1952) represent valuable contributions, Lighthill's work is the first to properly capture the inertial effects which propel high-*Re* swimmers. The core of Lighthill's contribution consists of his elongated-body theory of fish locomotion. Drawing upon analytical methods for the study of slender bodies such as airships, he constructs a compact model of swimming physics in the inertial regime. Under the assumption of small-amplitude swimming motions Lighthill (1960) demonstrates that swimming efficiency is determined by a single variable: the slip ratio (V/c). The slip ratio quantifies swimming velocity (V) relative to the backwards propagation speed c of the body wave, as shown in figure 1, where f is tailbeat frequency and λ is the wavelength of undulation. Lighthill found that as the slip ratio approaches one, efficiency rises to 100 % while thrust drops to zero. To minimize power consumption during locomotion, he concludes that animals must attempt to maximize V/c while maintaining enough thrust to overcome drag. The simplicity of this result is appealing; however, its applicability is limited by the small-amplitude restriction. Expanding on his previous work, Lighthill (1971) develops a large-amplitude version of elongated-body theory in which the performance of the swimmer is a function of both the slip ratio and the Strouhal number (St). This large-amplitude version of Lighthill's theory forms the core of the analysis presented here.

Twenty years after Lighthill's work, a shift in focus was brought about by the findings of Triantafyllou, Triantafyllou & Gopalkrishnan (1991). Triantafyllou observed a consistent wake morphology among swimming species with foil-like tails. During undulation, a vortex is shed at each reversal of the tail beat. This produces a series of counter-rotating vortices behind the animal, as shown in figure 1. In dimensionless terms, bluff body wakes are classically described using the Strouhal number, $St_b = fd/V$, where f is the frequency of vortex shedding, d is the diameter of the body, and V is flow velocity. Triantafyllou adapts St to describe the swimming wake by replacing body diameter with the amplitude of the tail beat, $St = 2fA/V$. In this form, St provides a simple but direct connection between the kinematics of a swimming animal and its trailing wake (Triantafyllou, Triantafyllou & Yue 2000). Triantafyllou *et al.* (1991) observed that swimming animals with foil-like tails adhere to a relatively narrow St range, $0.2 < St < 0.4$. Through experiments he then showed that the efficiency of an isolated flapping foil peaks at a similar value.

Many studies have since confirmed the observations of Triantafyllou; examples include the compiled datasets of Taylor, Nudds & Thomas (2003) and Rohr (2004). Although the significance of St is well established, the physical basis for the observed optimal range is still a topic of debate. Triantafyllou, Triantafyllou & Grosenbaugh (1993) propose that it is determined by the convective instability of the wake. During swimming, a shear flow profile is produced immediately behind the trailing edge of the tail – the unstable nature of this flow profile causes it to evolve into a vortex wake as it propagates away from the animal. Triantafyllou *et al.* (1993) explain that

https://doi.org/10.1017/jfm.2018.14 Published online by Cambridge University Press

the unstable wake acts as a tuned amplifier which magnifies the animal's perturbing tailbeat. Based on this, they suggest that swimming animals tune their motions to strengthen the efficient vortex wake by matching their kinematics to the resonant frequency of the wake dynamics. In recent work, Moored *et al.* (2012, 2014) test this hypothesis using experimental flow profiles produced by a flapping mechanical fin (Clark & Smits 2006). Moored *et al.* (2012, 2014) demonstrate that resonance conditions often do correspond to local peaks in efficiency. Based on these results, it is clear that wake resonance can influence the performance of flapping foils; further work is required to understand how these effects transfer to elongated animals.

Linden & Turner (2004) propose an alternative explanation for the *St* range of undulatory swimmers. Based on an analysis of vortex ring formation (Linden & Turner 2001), they suggest that swimming efficiency is not a function of bulk wake structure. Instead, it is proposed that thrust generation and power consumption are determined by the isolated properties of individual vortex rings within the wake. Linden and Turner hypothesize that swimming kinematics are chosen to produce optimal vortex rings which maximize their momentum while minimizing total kinetic energy. Dabiri (2009) discusses this hypothesis extensively in the context of jet-based propulsion as employed by squid and jellyfish, but a rigorous investigation of undulatory swimming has yet to be conducted from this perspective.

Triantafyllou's experiments use high-aspect-ratio flapping to foils to approximate the tails of scombrid fish such as tuna and mackerel or cetaceans such as dolphins and whales. These animals are among nature's fastest and most efficient swimmers, but they represent just a fraction of the full range of swimming species within the natural world. The analysis presented here considers swimming animals with slender elongated-body shapes that cannot be approximated as foils. Examples include salmonid fish such as trout and salmon or anguillids such as the American and European eel. The kinematics of elongated animals often deviate from the 0.2–0.4 *St* range and studies have shown that they produce a variety of complex wake morphologies which differ from the singular counter-rotating vortices of foil-tail swimmers (Muller *et al.* 2001; Tytell *et al.* 2010; Eloy 2012).

In an effort to understand the behaviour of these animals, a wide range of hydrodynamic models have been used to explore the complex relationship between kinematics, efficiency, and swimmer geometry. In their full form, these relationships are governed by a three-dimensional interaction between the swimmer's body and the surrounding fluid. A number of studies have applied computational methods to directly simulate this three-dimensional system. Examples include the work of Kern & Koumoutsakos (2006), which applies evolutionary optimization methods to identify efficient and high-velocity swimming motions for a three-dimensional anguilliform swimmer; van Rees, Gazzola & Koumoutsakos (2013), which applies a similar approach to study optimal body shapes with imposed kinematics; van Rees, Gazzola & Koumoutsakos (2015), which considers optimal body shape and kinematics simultaneously; and the work of Maertens, Gao & Triantafyllou (2017), which considers optimal kinematics and fish schooling interactions.

A number of studies have also applied reduced order models to study swimming systems. Although this approach cannot provide the detailed flow visualizations of full computational methods, the transparency of these simplified models has produced a number of significant insights. Gazzola, Argentina & Mahadevan (2014) constructs a simple scaling argument to explain why the kinematics of intermediate-*Re* swimmers differ from those at high *Re*, Tokić & Yue (2012) apply Lighthill's elongated-body theory in combination with numerical optimization to accurately predict form and

https://doi.org/10.1017/jfm.2018.14 Published online by Cambridge University Press

behaviour for a range of different swimming species, and Eloy (2012, 2013) uses a similar approach to demonstrate that optimal St varies systematically with the body drag and tail size of swimming animals.

Here, we build upon the findings of Eloy (2012). Using Lighthill's large-amplitude elongated-body theory, we show that optimally efficient swimming kinematics can be reduced to a single dimensionless variable, ψ, which is defined by a simple function of a swimming animal's body wave properties. This variable, ψ, characterizes how the velocity of the animal's tail varies in time as it beats back and forth through the surrounding fluid. Using Lighthill's model, we show that regardless of a swimming animal's size and shape, peak efficiency is always achieved at $\psi = 0.87$. At this point, the average magnitude of the tail velocity is minimized and the animal produces a relatively constant thrust coefficient throughout its swimming stroke. We use a compiled dataset of over 250 unique measurements of swimming animals to show that species across a wide range of size and shape follow the predicted optimum.

The current understanding of efficient swimming at high Re is founded upon Triantafyllou's pioneering work on vortex shedding and flapping foils. Triantafyllou demonstrated that lunate tail swimmers adhere to a narrow optimal St range of 0.2–0.4, where they produce a characteristic vortex wake. Biological measurements have since confirmed that St plays a critical role in the behaviour of swimming animals across a wide range of morphologies, but it is currently unclear how Triantafyllou's results translate to slender animals with elongated tails. Within Lighthill's model, we find that optimality is entirely determined by the variable ψ; St is instead determined by thrust–drag balance. While $\psi = 0.87$ characterizes the optimal undulation pattern for efficient swimming, St scales the magnitude of this pattern, such that the thrust output of the tail can be adjusted to match the drag of the body.

2. Constructing the swimming model

We begin by establishing the details of the swimming model applied throughout our analysis. The model description is divided into three subsections: (1) geometry and kinematics, (2) Lighthill's large-amplitude elongated-body theory, and (3) thrust and power consumption during steady swimming.

2.1. *Geometry and kinematics*

Throughout our analysis we refer to slender swimmers as being distinct from foil-tailed animals. Slender swimmers are characterized by a low aspect ratio, $AR = h/L$, and slowly varying cross-sectional shape, where h is the height of the trailing edge and L is body length. In figure 2, we compare the body forms of an eel-, a trout-, and a tuna-like swimmer. Since Lighthill's model assumes a slender geometry, our analysis is applicable to animals with shapes similar to the eel and trout, but not the tuna, which exhibits a distinct foil-like tail.

Within Lighthill's elongated-body theory, the thrust and power consumption of a swimming animal are fully determined through the motion of its trailing edge. To define the kinematics at this point, we apply the definition of Eloy (2012). The swimmer is assumed to travel forward at a constant velocity V and the trailing edge is prescribed to undergo periodic heaving and pitching with a phase lag of π between the two motions. This approximates the wave-like tail motion of natural swimmers as shown in figure 1 (Lighthill 1969). The resulting kinematics are defined through the position $\boldsymbol{r}(t)$ and angle $\theta(t)$ of the tail, shown in figure 2 and given as

$$\boldsymbol{r}(t) = Vt\hat{\boldsymbol{e}}_x + A\cos(2\pi ft)\hat{\boldsymbol{e}}_y \quad \text{and} \quad \theta(t) = \beta\sin(2\pi ft). \tag{2.1a,b}$$

https://doi.org/10.1017/jfm.2018.14 Published online by Cambridge University Press

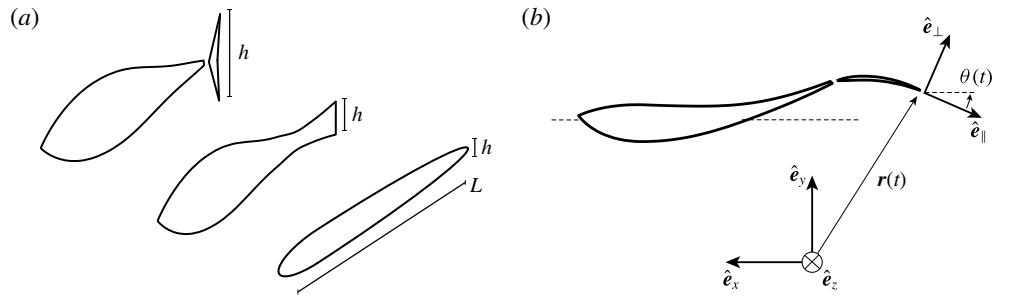


FIGURE 2. (*a*) Comparison of slenderness (h/L) for tuna-, trout-, and eel-type swimmers. (*b*) Coordinate frames and functions used to describe the motion of the swimmer.

These kinematics are characterized by four parameters: frequency (f), amplitude (A), pitching angle (β), and velocity (V). These parameters reduce to two dimensionless groups, pitch angle β and the Strouhal number $St = 2fA/V$. If we assume the path of the tail approximates a sinusoidal wave, pitch angle can be related to Lighthill's slip ratio as follows (see appendix A for a derivation of this relation):

$$\beta = \pi \frac{V}{c} St. \tag{2.2}$$

Here, we often use the slip ratio, V/c, in place of β, as V/c is widely used in previous studies.

To quantify the thrust and power consumption of the swimmer we need to determine the tangential and normal components of the trailing edge velocity. They can be calculated by taking the time derivative of the position vector, $\boldsymbol{r}$, and projecting the result on to $\hat{\boldsymbol{e}}_\perp$ and $\hat{\boldsymbol{e}}_\parallel$ as follows:

$$v_\perp = \frac{\mathrm{d}\boldsymbol{r}}{\mathrm{d}t} \cdot \hat{\boldsymbol{e}}_\perp \quad \text{and} \quad v_\parallel = \frac{\mathrm{d}\boldsymbol{r}}{\mathrm{d}t} \cdot \hat{\boldsymbol{e}}_\parallel. \tag{2.3a,b}$$

We then non-dimensionalize $v_\perp$ and $v_\parallel$ against the swimming velocity V and normalize time against the swimming frequency. This produces the following expressions:

$$v_\perp^* = \frac{v_\perp}{V} = -\pi St \cos(\beta \sin(t^*)) \sin(t^*) + \sin(\beta \sin(t^*)), \tag{2.4}$$

$$v_\parallel^* = \frac{v_\parallel}{V} = -\pi St \sin(\beta \sin(t^*)) \sin(t^*) - \cos(\beta \sin(t^*)), \tag{2.5}$$

where $t^* = 2\pi ft$.

2.2. *Fluid forces*

Within Lighthill's large-amplitude elongated-body theory (Lighthill 1971), the thrust produced by a swimmer ($\overline{T}$) is given by the streamwise projection of a normal force, $\boldsymbol{F}_n$, and a tangential force, $\boldsymbol{F}_t$. The normal force is produced by the inertial reaction of the fluid as the swimmer's body undulates back and forth. The source of the tangential force is somewhat less intuitive. Lighthill (1971) demonstrates its existence through an energy balance, while Wu (1971) arrives at the same result by integrating over a leading edge singularity within the flow field around the swimmer's tail. To calculate

https://doi.org/10.1017/jfm.2018.14 Published online by Cambridge University Press

the average thrust generated over a complete a swimming cycle, we integrate the thrust over one full period, producing the following result, where ρ is fluid density. The notation used here is different from that of Lighthill (1971); the equivalency of our definitions is demonstrated in appendix C.

$$\overline{T} = f \int_0^{1/f} (\boldsymbol{F}_n(t) + \boldsymbol{F}_t(t)) \cdot \hat{\boldsymbol{e}}_x \, \mathrm{d}t, \tag{2.6}$$

$$\boldsymbol{F}_n(t) = \frac{\pi}{4} \rho V^2 h^2 \, (v_\parallel^* v_\perp^*) \hat{\boldsymbol{e}}_\perp, \tag{2.7}$$

$$\boldsymbol{F}_t(t) = \frac{\pi}{4} \rho V^2 h^2 \left(\frac{1}{2} v_\perp^{*2} \right) \hat{\boldsymbol{e}}_\parallel. \tag{2.8}$$

The thrust integral of (2.6) is used to define a dimensionless thrust coefficient, $C_T(V/c, St)$, given as

$$\overline{T} = \tfrac{1}{2} \rho V^2 h^2 C_T, \tag{2.9}$$

$$C_T = \frac{1}{4} \int_0^{2\pi} \left(v_\parallel^* v_\perp^* \sin(\theta(t^*)) + \frac{1}{2} v_\perp^{*2} \cos(\theta(t^*)) \right) \mathrm{d}t^*. \tag{2.10}$$

2.3. *Thrust–drag balance during steady swimming*

During constant-velocity swimming, the average thrust produced by the swimmer must be balanced by the drag of its body. This requirement is enforced by defining a drag force, D, and setting $\overline{T}/D$ to be equal to one:

$$\frac{\overline{T}}{D} = C_T \left(\frac{\frac{1}{2} \rho V^2 h^2}{D} \right) = 1. \tag{2.11}$$

The first term in this expression is the thrust coefficient. The second term, contained in parentheses, represents a ratio of the total drag on the fish and the thrust-generating capability of the tail. Following Eloy (2012) we refer to this ratio as the Lighthill Number, Li. Applying this definition reduces thrust–drag equilibrium to a simple dimensionless constraint:

$$C_T = Li, \quad \text{where } Li = \frac{D}{\frac{1}{2} \rho V^2 h^2}. \tag{2.12}$$

Physically, Li represents the tail loading of the swimmer in a similar sense to the wing loading of a bird or insect. A swimming animal with a small Li value would have a relatively large tail in relation to the drag of its body, while the tail of a high-Li animal would be relatively small.

2.4. *Power and efficiency*

During swimming, energy generated by a swimmer's muscles is dissipated through two distinct power sinks: useful thrust power, and kinetic energy left behind in the trailing wake. Following Lighthill, these can be quantified as

$$P_{thrust} = \overline{T} V, \quad P_{wake} = -\frac{1}{8} \rho V^3 h^2 \int_0^{2\pi} \left(\frac{1}{2} v_\parallel^* v_\perp^{*2} \right) \mathrm{d}t^*. \tag{2.13a,b}$$

https://doi.org/10.1017/jfm.2018.14 Published online by Cambridge University Press

As proposed by Lighthill, we define the efficiency of the swimmer as a ratio of useful thrust power over the total power consumed by the animal:

$$\eta = \frac{\overline{T}V}{\overline{T}V + P_{wake}}. \tag{2.14}$$

If we non-dimensionalize both the numerator and denominator then divide through by $C_T V$, efficiency reduces to the following, where C_P is the dimensionless form of the wasted wake power (P_{wake}):

$$\eta = \frac{1}{1 + C_P/C_T}, \quad \text{where } C_P = -\frac{1}{4}\int_0^{2\pi} \left(\frac{1}{2} v_\parallel^* v_\perp^{*2}\right) \mathrm{d}t^*. \tag{2.15}$$

3. Optimally efficient swimming kinematics

At this stage we have fully defined and non-dimensionalized our swimming system. From (2.15), we see that the efficiency of the swimmer is solely determined through a ratio of the power and thrust coefficients C_P/C_T. Using this result we can formally state the efficiency optimization problem as follows:

$$\underset{V/c,\, St}{\text{Minimize}} \quad C_P = -\frac{1}{4}\int_0^{2\pi} \frac{1}{2} v_\parallel^* v_\perp^{*2}\, \mathrm{d}t^* \tag{3.1}$$

$$\text{subject to} \quad \frac{C_T}{Li} = \frac{1}{4}\int_0^{2\pi} \frac{(v_\parallel^* v_\perp^* \sin(\theta(t^*)) + \frac{1}{2} v_\perp^{*2} \cos(\theta(t^*)))}{Li}\, \mathrm{d}t^* = 1. \tag{3.2}$$

The resulting problem is equivalent to that of Eloy (2012). In total, it contains three variables (V/c, St, Li) and one constraint ($C_T = Li$). Eloy (2012) solves the problem numerically to determine the optimal relationship between the kinematic variables (St, V/c) and the tail loading (Li).

To assess the validity of the predicted relationships, Eloy (2012) compares them to observed animal behaviour. He approximates the value of Li for a given species by assuming that swimming drag arises predominantly through skin friction, such that $D = 1/2\rho C_f V^2 S$, where C_f is a frictional drag coefficient and S is the surface area of the animal. Through this comparison Eloy demonstrates that Lighthill's model correctly predicts the $St - Li$ relationship of swimming animals. For V/c and Li the match is much weaker; this inconsistency can be attributed to the difficulties in determining accurate numerical values for Li. Realistically, swimming drag (D) is a complex function of shape, surface area and kinematics, and effects beyond skin friction may significantly contribute to its overall magnitude (Raspa *et al.* 2014).

Here, we consider the solution as an optimal relationship between St and V/c. In this form, it can be compared to animal data without the need to approximate Li. Assuming that a swimming animal must generate some finite amount of thrust, Lighthill's model predicts that efficient swimmers should tune their kinematics to fall along the optimal $St - V/c$ curve. In figure 3 we plot this curve against a compiled dataset of over 250 unique observations of swimming kinematics for the 13 different animal species listed in table 1. Data points corresponding to trout, goldfish and sturgeon are highlighted with unique symbols as they constitute the bulk of the data. Through this comparison we see that the data points are distributed along the optimally efficient region, confirming Eloy's finding that slender swimming animals

https://doi.org/10.1017/jfm.2018.14 Published online by Cambridge University Press

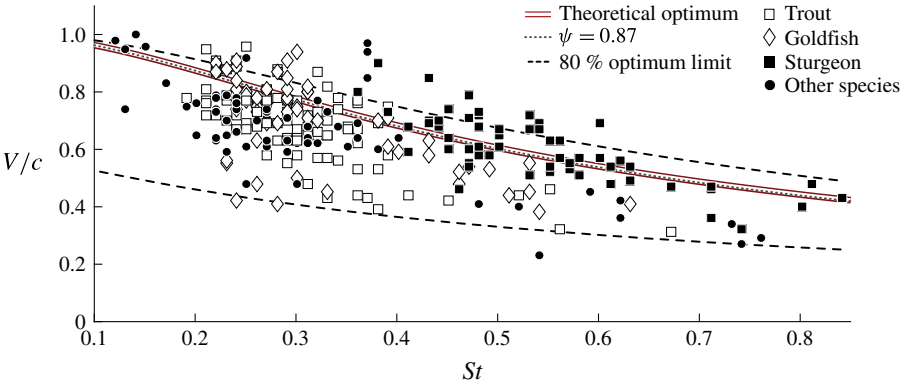


FIGURE 3. (Colour online) Comparison of optimal behaviour within Lighthill's model and the observed St and V/c of natural swimmers. Dashed lines bracket the region where swimming efficiency is at least 80 % of its peak value for a given thrust coefficient. A list of the species within the dataset is provided in table 1. The raw dataset and further details on its contents are available online.

Species	Source	Data points
Trout (*Oncorhynchus mykiss*)	Bainbridge (1958)	82
Goldfish (*Carassius auratus*)	Bainbridge (1958)	41
Goldfish (*Carassius auratus*)	Blake, Li & Chan (2009)	16
Largemouth bass (*Micropterus salmoides*)	Jayne & Lauder (1995)*	5
Mosquitofish (*Gambusia affinis*)	Langerhans (2009)	6
Atlantic needlefish (*Strongylura marina*)	Liao (2002)*	3
Longnose gar (*Lepisosteus osseus*)	Long *et al.* (1996)	7
Cod (*Gadus morhua*)	Videler & Wardle (1978)	6
Saithe (*Pollachius virens*)	Videler & Hess (1984)	13
Great sand eel (*Hyperoplus lanceolatus*)	Videler (1993)*	5
Lesser sand eel (*Ammodytes marinus*)	Videler (1993)*	4
Atlantic salmon (*Salmo salar*)	Videler (1993)*	3
Blacktip shark (*Carcharhinus melanopterus*)	Webb & Keyes (1982)	15
Trout (*Oncorhynchus mykiss*)	Webb, Kostecki & Stevens (1984)*	9
Lake sturgeon (*Acipenser fulvescens*)	Webb (1986)	57

TABLE 1. List of species within the compiled dataset. Data sources marked with a * are taken from the compilation of van Weerden, Reid & Hemelrijk (2014).

do not always adhere to the 0.2–0.4 St range. Instead, it suggests that they adhere to an optimal $St - V/c$ relationship, with the exact position along this curve determined by the animal's required thrust coefficient.

The raw dataset and further details on its contents are supplementary materials available online at https://doi.org/10.1017/jfm.2018.14. Constructing a meaningful dataset is a challenging process, as many if not most of the available studies on swimming kinematics are conducted using enclosed flow channels which can influence swimming behaviour and it can be difficult to determine whether swimming efficiency is a strong motivator for a given fish species. Nonetheless, considering the dataset as a whole, we see a clear trend along the predicted optimal region. Furthermore, the

https://doi.org/10.1017/jfm.2018.14 Published online by Cambridge University Press

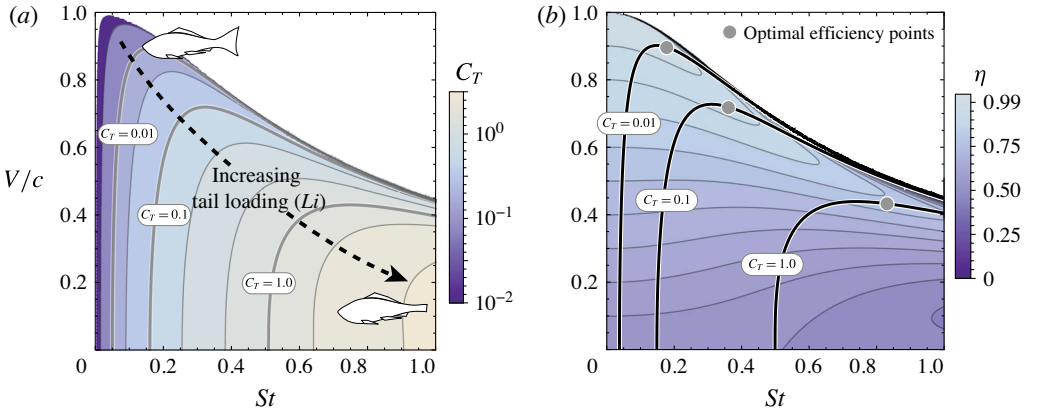


FIGURE 4. (Colour online) (*a*) Thrust coefficient plotted over a grid of slip and Strouhal values. A swimming animal with a given tail loading (*Li*), is constrained to kinematics along a single level C_T curve. (*b*) Froude efficiency plotted over the same grid. The overlaid curves illustrate the constraint between V/c and *St* during steady swimming.

three species with the largest number of data points (trout, goldfish, and sturgeon) all exhibit swimming behaviours which fall outside the 0.2–0.4 *St* range, but sit along the optimal curve.

4. The physical basis of efficient swimming within Lighthill's model

Having established that Lighthill's model predicts both *St* and V/c for slender swimmers, in the following section we dissect this result to understand the physical effects which drive the optimal curve. Through this process we find that efficient swimmers tune their movements to minimize the average magnitude of $v_\perp$ and to produce an instantaneous thrust coefficient which varies as little as possible throughout the tailbeat.

To show this, we begin by examining the underlying structure of the problem. In figure 4(*a*), the thrust coefficient, C_T, is plotted over the V/c–*St* plane. The thrust–drag constraint ($C_T = Li$) is visualized through the resulting contours. An animal with tail size, *h*, swimming with body drag *D* has a fixed value of *Li*. Consequently, it is constrained to use kinematics along the corresponding C_T contour. From the plot we see that C_T increases towards the bottom right corner, indicating that swimmers in this region must have small tails and large bodies, while the opposite is true in the upper left. Kinematics within the blank segment of the plot can be ignored as C_T is negative within this region.

In figure 4(*b*), we plot the efficiency of the swimmer over the same grid. The plot exhibits relatively horizontal bands, with efficiency tending towards a maximum as V/c approaches 1. To demonstrate how *St* impacts efficiency, we must consider the thrust–drag constraint ($C_T = Li$). Since an animal swimming with body drag *D* is restricted to a single C_T curve, *St* and V/c are not independent. Superimposing the constant thrust contours onto the efficiency plot, we see that efficiency is poor at the high and low *St* limits of each curve, where slip converges to zero; between these two limits there is a narrow *St* range where V/c is maximized and efficiency is high. The animal data in figure 3 show that natural swimmers choose their kinematics to sit in this optimal region along the peaks of the constant thrust contours.

https://doi.org/10.1017/jfm.2018.14 Published online by Cambridge University Press

To get a sense of the physical effects which drive this structure we consider the form of the thrust and power coefficients. Within Lighthill's model, swimming animals produce thrust through two distinct sources: a normal force from the acceleration of fluid mass ($\boldsymbol{F}_n$) and a tangential force ($\boldsymbol{F}_t$). In the vicinity of the optimum, the normal force dominates the efficient swimming problem (see appendix B). Based on this we examine a reduced thrust-to-power ratio:

$$\frac{C_T}{C_P} \approx \frac{C_n}{C_P} = \frac{\displaystyle\int_0^{2\pi} v_\parallel^* v_\perp^* \sin(\theta(t^*))\,\mathrm{d}t^*}{\displaystyle\int_0^{2\pi} -\frac{1}{2} v_\parallel^* v_\perp^{*2}\,\mathrm{d}t^*}. \tag{4.1}$$

In this form the optimal swimming problem is dependent on three unique terms, $v_\parallel^*$, $v_\perp^*$, and $\sin(\theta(t^*))$. $v_\parallel^*$ appears linearly in both the thrust and power integrals and thus has relatively little effect on overall swimming efficiency. Instead, the dominant role is played by $v_\perp^*$. With $\boldsymbol{F}_n$ as the dominant thrust source, the constraint ($C_T = Li$) scales linearly in $v_\perp^*$, while the objective (C_P) scales quadratically. To gain insight into this problem form, we consider a similar system given as follows:

$$\underset{f(z)}{\text{Minimize}} \quad F_{cost} = \int_0^1 f^2(z)\,\mathrm{d}z \tag{4.2}$$

$$\text{subject to} \quad F_{output} = \int_0^1 f(z)\,\mathrm{d}z = G, \tag{4.3}$$

where G is a constant and $f(z)$ is an arbitrary real function. If we substitute the trial solution $f(z) = G + \epsilon(z)$, we find that $\epsilon(z) = 0$. In physical terms this means that any variation in the output of the system will tend to increase the overall cost of that output. Transferring this reasoning to our problem suggests that its form penalizes variations within $v_\perp^*$. Efficiency optimization should favour kinematics which maintain a relatively constant thrust coefficient throughout the swimming motion.

Based on this, swimming kinematics which generate strong peaks in $v_\perp^*$ should be inefficient, while those that yield a relatively flat $v_\perp^*$ profile should minimize energy consumption. We examine this relationship in figure 5(*b–d*), where $v_\perp$ profiles are plotted at three different points of the $C_T = 0.01, 0.1, 1$ contours. Since the swimming motion is antisymmetric about $t^* = \pi$, we show only the first half of the tailbeat cycle ($t^* = 0 - \pi$). When St is less than the optimal value, the profile exhibits a single large peak throughout each stroke of the tail. When St is greater than the optimal value, a large negative trough appears in the centre of each stroke. The optimal St value provides a balance between the two limits, producing a profile which oscillates near a mean constant value.

The steadiness of the thrust coefficient can be characterized by comparing its instantaneous value, C_T^i, to its average value, C_T. This is accomplished through the following metric, Δ, which quantifies the mean variation in C_T over each half of the tail beat:

$$\Delta = \frac{1}{\pi C_T} \int_0^\pi |C_T^i - C_T|\,\mathrm{d}t^*. \tag{4.4}$$

In figure 5(*e*), Δ is plotted along the $C_T = 0.01$, 0.1, and 1 contours. The resulting curves show that the optimal stroke minimizes the variation of C_T across all thrust levels.

https://doi.org/10.1017/jfm.2018.14 Published online by Cambridge University Press

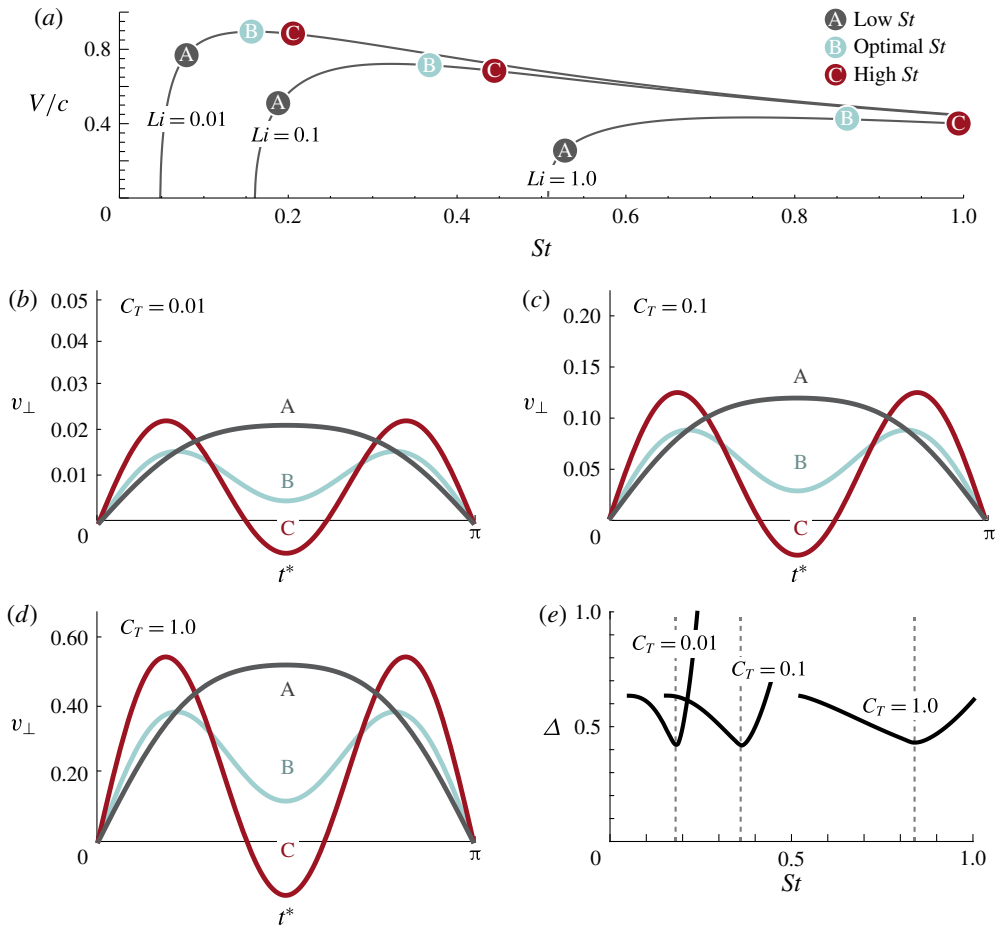


FIGURE 5. (Colour online) (*a*) Points are used to identify three distinct swimming regimes along the $C_T = 0.01,\ 0.1,\ 1$ contours. (*b–d*) Comparison of $v_\perp^*$ profiles for each of the three swimming regimes. (*e*) Thrust coefficient variation, Δ, plotted along constant thrust contours. Dashed lines mark points of maximum efficiency.

Conceptually, the kinematics of the optimal solution are similar to the twisted design of a propeller blade. As a propeller rotates, blade sections at the outer radius move faster than those at the inner radius. To counter this effect, each blade is axially twisted such that pitch decreases towards the tip. This allows the propeller to maintain a constant angle of attack along its entire length (von Mises 1959). In the case of fish, the velocity of the tail tip varies in time rather than space, but kinematics are tuned to achieve a similar effect. The time-varying pitch of the tail balances changes in lateral velocity such that the thrust coefficient remains relatively constant throughout the full tail beat.

In addition to minimizing variations in C_T, kinematics along the optimal curve also tend to minimize the average magnitude of $v_\perp^*$. We demonstrate this in figure 6(*a*), where we plot the average value of $v_\perp^*$ along the constant thrust contours. If we consider the form of the thrust output in (4.1), ($C_T = \int_0^{2\pi} v_\parallel^* v_\perp^* \sin(\theta(t^*))\,\mathrm{d}t^*$), we see that $v_\perp^*$ can be minimized by swimming with a large tail pitch, $\theta(t^*)$, to maximize the

https://doi.org/10.1017/jfm.2018.14 Published online by Cambridge University Press

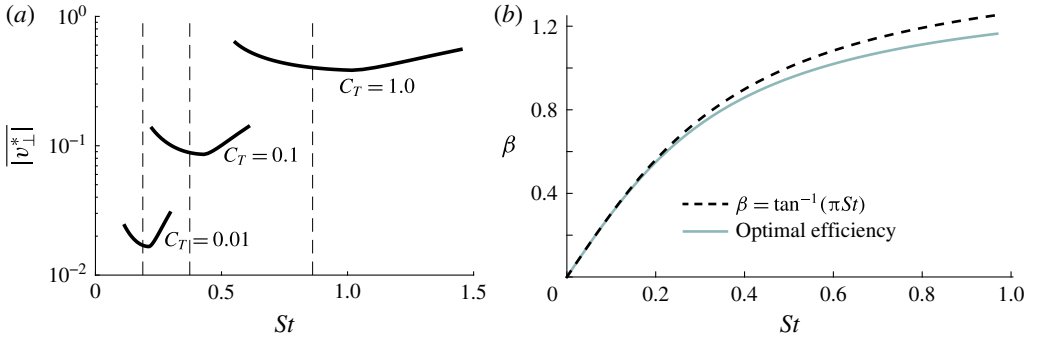


FIGURE 6. (Colour online) (*a*) Average magnitude of $|v_\perp^*|$ plotted along constant thrust contours. Dashed lines mark the point of optimal efficiency along each contour. (*b*) Comparison of the negative thrust threshold and the optimal efficiency curve in the β–St plane.

projected thrust component of the fluid momentum shed from the tail. However, if the pitch amplitude is too large, $v_\perp^*$ can become negative at the midpoint of the tailbeat. This can be observed in the high-St profiles of figure 5. During periods where $v_\perp^*$ is less than zero, the swimmer produces negative thrust, effectively increasing the overall drag of its body and severely reducing swimming efficiency. The pitch amplitude associated with the onset of negative thrust production can be calculated by setting $v_\perp^*$ equal to 0 at $t^* = \pi/2$. This produces the following relation:

$$\beta = \tan^{-1}(\pi St). \tag{4.5}$$

In figure 6(*b*) we compare this relation to the efficiency optimum, in the β–St plane. From the resulting curves we see that the optimum runs alongside the negative thrust limit. Swimming kinematics in this region maximize the projected thrust component while avoiding periods of negative thrust production.

4.1. *Non-harmonic swimming motions*

Taking the idea of minimal thrust variation to its limit, a swimming motion which produces perfectly constant thrust should provide the highest possible efficiency. Inspecting the form of our optimization problem, we can see that it supports this hypothesis. The integrands defining the thrust and power coefficients in (3.1) and (3.2) are purely dependent on the instantaneous state of the system. Based on this, it should be possible to maximize efficiency by identifying the tail angle and velocity which minimize power consumption on an instantaneous basis and then maintaining these values throughout each complete stroke of the tail. This motion can be produced by using square waves to define the lateral velocity, $\mathrm{d}y/\mathrm{d}t$, and tail pitch, θ, such that the tail tip traces out a triangular path. In a sense, this result is the high-Reynolds-number equivalent of Lighthill's optimal triangle wave for low-Reynolds-number swimmers (Lighthill 1975).

We parametrize this triangle wave such that it is consistent with the rest of our analysis. The constant lateral velocity is defined as $\mathrm{d}y/\mathrm{d}t = 2\pi f A_c$, which becomes $\mathrm{d}y/\mathrm{d}t = \pi St_c$ when non-dimensionalized against forward velocity V and the constant pitch is defined as $\theta = \beta_c$. Imposing these motions reduces the thrust and power

https://doi.org/10.1017/jfm.2018.14 Published online by Cambridge University Press

integrals of (3.1) and (3.2) to simple constants. We can exploit this simplification to analytically solve for the optimal properties of our triangular tail beat as a function of Li. To do this, we use the thrust constraint $C_T = Li$ to eliminate St_c from the power coefficient and then differentiate the result to solve for the optimal value of β_c as follows:

$$\frac{\partial}{\partial \beta_c}(C_P(\beta_c, Li)) = 0. \tag{4.6}$$

Solving this equation, we find that efficiency is maximized as St_c approaches zero and β_c approaches $\pi/2$. This corresponds to the tail moving vertically with $v_\perp$ near zero and compensating with $v_\parallel$ near infinity, to generate a finite amount of thrust. At this point, efficiency approaches 100 % for all values of Li. Clearly, this is not physically meaningful; in reality, factors neglected by Lighthill's model would make this motion highly inefficient. Nonetheless, this insight is useful in understanding the results presented here. Throughout our analysis the movement of the tail is restricted to a more physically feasible range of sinusoidal motions; Lighthill's model predicts that a swimmer is most efficient when it tunes these motions to approximate the constant thrust of a triangular wave.

5. A self-similarity along the optimum

Comparing the $v_\perp^*$ profiles presented in figure 5 reveals a self-similarity within the optimal swimming problem; the profiles along the higher thrust curves appear to be scaled versions of those at lower thrust values. In the following section, we exploit this insight to construct a similarity variable, ψ, which uniquely characterizes the $v_\perp^*$ profile of a swimming animal. Using this variable, we then show that the optimal V/c–St relationship collapses to a simple constant $\psi = 0.87$. This point corresponds to a single optimal $v_\perp^*$ profile, common to all slender swimming animals.

To construct our similarity variable, ψ, we begin by selecting a scalar property which uniquely identifies the different $v_\perp^*$ profiles along each thrust curve. In figure 7(*a*) we see that the magnitude of $v_\perp^*$ at $t^* = \pi/2$ decreases monotonically as St increases. We verify this in figure 7(*b*), where $v_\perp^*|_{t^*=\pi/2}$ is plotted along three different thrust contours. To collapse these curves to a single line, we normalize $v_\perp^*|_{t^*=\pi/2}$ against its derivative at $t^* = 0$:

$$\psi' = v_\perp^*|_{t^*=\pi/2} \left(\left. \frac{\partial v_\perp^*}{\partial t} \right|_{t^*=0} \right)^{-1}. \tag{5.1}$$

The collapsed curves are shown in figure 7(*c*). To complete our similarity variable, we make one last change. Profile shapes relevant to natural swimmers correspond to the range $-\infty < \psi' < 1$. We apply a change of variables to alter this range to $0 < \psi < \infty$ for the sake of convenience. This yields the final result:

$$\psi = 1 - \frac{\sin(\beta) - \pi St \cos(\beta)}{\beta - \pi St}, \quad \text{where } \beta = \pi \frac{V}{c} St. \tag{5.2}$$

In figure 8, we can now see that each value of ψ corresponds to a single common $v_\perp^*$ profile across all thrust contours.

5.1. *Solving for optimal* ψ

If the optimal V/c–St relationship corresponds to a line of fixed profile shape it should reduce to a constant, $\psi = \psi_{opt}$. To solve for the value of this constant we consider the

https://doi.org/10.1017/jfm.2018.14 Published online by Cambridge University Press

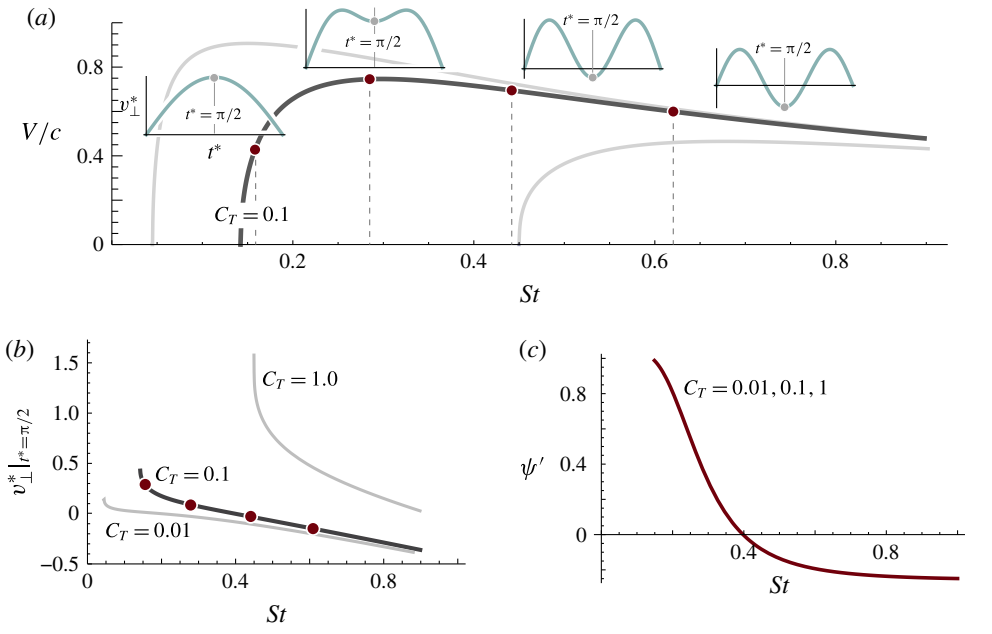


FIGURE 7. (Colour online) (*a*) The value $v_\perp^*$ at $t^* = \pi/2$ is unique for each point along a given constant thrust curve. (*b*) Curves of $v_\perp^*|_{t^*=\pi/2}$ versus *St* illustrate the one-to-one mapping between $v_\perp^*|_{t^*=\pi/2}$ and profile shape along each thrust curve. (*c*) Normalizing $v_\perp^*|_{t^*=\pi/2}$ collapses the curves from the plot in (*b*) to a single line.

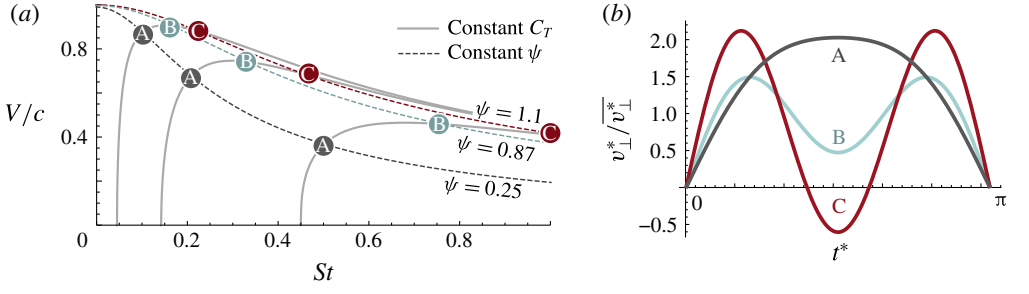


FIGURE 8. (Colour online) Each value of ψ corresponds to a single self-similar $v_\perp^*$ profile across all thrust contours. Each set of V/c–*St* points identified in (*a*) corresponds to a $v_\perp^*$ profile plotted in (*b*).

form of the thrust and power coefficients. When expressed in terms of β and *St* they consist of polynomials in *St* with coefficients defined by nonlinear functions of β:

$$C_T(\beta, St) = f_2(\beta)St^2 + f_1(\beta)St + f_0(\beta), \tag{5.3}$$

$$C_P(\beta, St) = g_3(\beta)St^3 + g_2(\beta)St^2 + g_1(\beta)St + g_0(\beta). \tag{5.4}$$

At the optimum, the gradient of the objective, C_P, is orthogonal to the constraint, $C_T = Li$, giving the following optimality condition:

$$\nabla C_P \cdot \boldsymbol{R} \nabla C_T = 0, \quad \text{where } \boldsymbol{R} = \begin{bmatrix} 0 & -1 \\ 1 & 0 \end{bmatrix}. \tag{5.5}$$

https://doi.org/10.1017/jfm.2018.14 Published online by Cambridge University Press

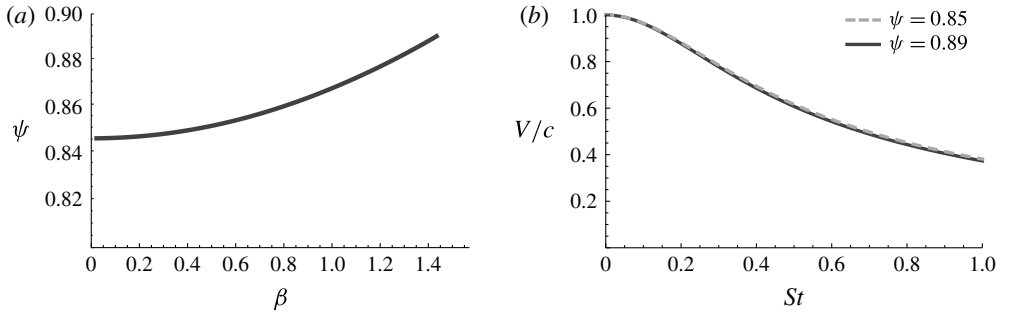


FIGURE 9. (*a*) Optimally efficient value of ψ, plotted as a function of β. (*b*) Comparison of the two limits bracketing the optimal solution. The resulting curves are nearly indistinguishable in the V/c–St plane.

Using this condition in combination with equations (5.2)–(5.4), we can solve for ψ_{opt} in terms of the tail pitch β. From the resulting solution, $\psi_{opt} = f(\beta)$, we find that the optimum is not analytically self-similar, but the variation in ψ_{opt} is small enough to be ignored for all practical applications. In figure 9(*a*), the value of ψ_{opt} is plotted over the range of tail pitch relevant to swimming animals, $0 < \beta < \pi/2$. From the resulting curve we see that ψ_{opt} varies from 0.85 to 0.89 with a mean value of 0.87. In figure 9(*b*), the bounds of ψ_{opt} are plotted in the V/c–St plane, where we can see that they nearly overlap one another. In figure 3, we plot the curve defined by $\psi = 0.87$ overtop the numerical optimum; the resulting comparison shows that the two solutions are effectively identical.

5.2. *Animal behaviour in terms of ψ and St*

To complete our analysis we revisit the behaviour of natural swimmers in the context of our similarity variable. In figure 10, the animal dataset is presented in terms of ψ and St. From the resulting plot we see that animal behaviour is distributed along the optimum at $\psi = 0.87$, and appears to be independent of St, as predicted. There is a relatively large degree of scatter, but this is to be expected given that we have used the slip ratio to approximate the tail pitch of the animals. As stated earlier, slip often varies along the length of the body and different methods of quantifying slip can influence the measured value by up to 10 %–20 % (Webb *et al.* 1984).

In figure 10(*b*), we plot a histogram of ψ for the complete dataset. The resulting distribution exhibits a clear peak in the efficient region and is well approximated by a normal distribution centred at $\psi = 0.58$ with the range $\psi = 0.28$–1.28 corresponding to plus or minus one standard deviation (S.D) from the mean. The ± 1 S.D. bounds are depicted in each of figure 10(*a–c*) to illustrate their form in the ψ–St and V/c–St planes. The peak at $\psi = 0.58$ differs from the optimal value of $\psi = 0.87$; this can be explained by considering how efficiency varies in relation to ψ. In figure 11(*a*) we plot the relationship between efficiency (η) and ψ for three different levels of thrust output. The resulting curves converge to 50 % efficiency at $\psi = 0$ and drop to 0 % efficiency at $\psi \approx 1.27$, with a broad plateau between these limits. The sharp drop in efficiency past $\psi = 1$ is caused by the onset of drag production at the tail. Using equation (5.2) it can be shown that $\psi = 1$ corresponds to the negative thrust threshold defined in (4.5). As discussed in § 4, this threshold marks the point where $v_\perp^*|_{t^*=\pi/2}$ drops below zero and the animal begins to generate negative thrust. When swimming at the theoretically optimal value of $\psi = 0.87$, small changes in kinematics can push an animal into this drag production region. We hypothesize that animals

https://doi.org/10.1017/jfm.2018.14 Published online by Cambridge University Press

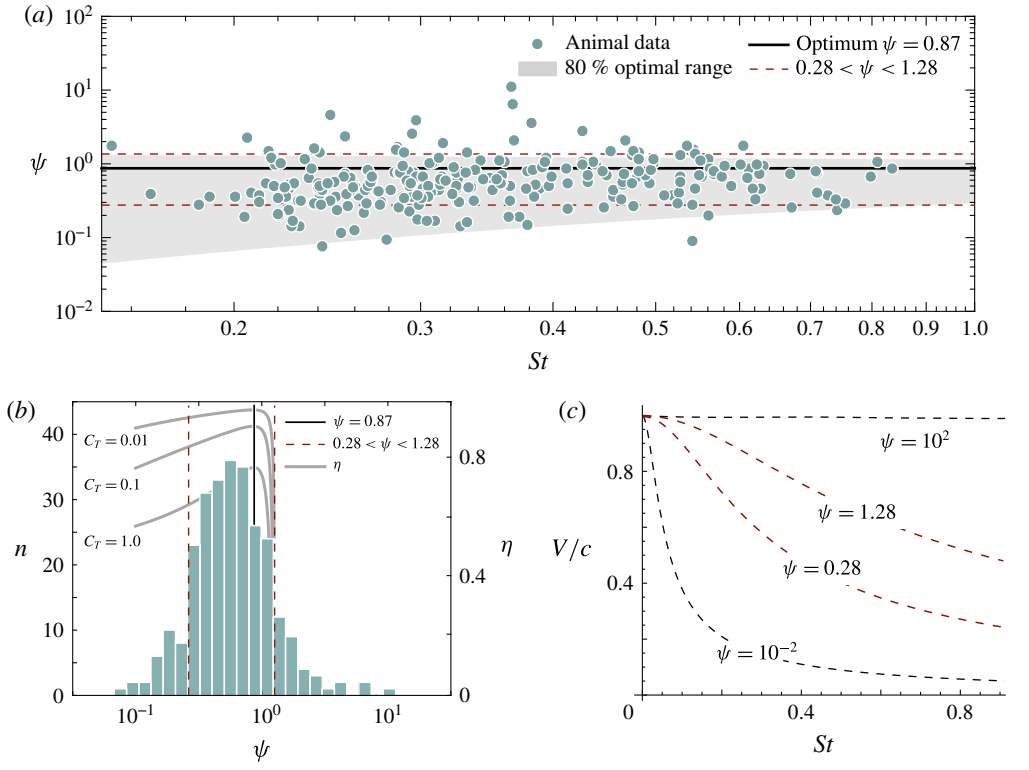


FIGURE 10. (Colour online) (*a*) Animal data mapped to the ψ–*St* plane. (*b*) Histogram of ψ values from animal data ($n_{total} = 272$). Efficiency curves are overlaid in grey. (*c*) Lines of constant ψ in the V/c–*St* plane are shown to justify the logarithmic scale used for ψ.

insulate themselves from this effect by choosing slightly lower ψ values. In this range efficiency is still close to optimal, but far more robust to kinematic deviations.

As highlighted earlier, optimally efficient swimmers tend to minimize both the average magnitude of $v_\perp^*$ and variations in thrust output C_T^i. In figure 11(*c*,*d*) we plot these quantities along lines of constant thrust, over a range of ψ values. From the resulting curves we see that both quantities exhibit a relatively flat region near the optimum at $\psi = 0.87$. This is consistent with the broad efficiency plateaus shown in the top left. Although there is a single mathematically optimal $v_\perp^*$ profile, in practical terms there is actually a range of self-similar profiles which provide near-optimal performance. The limits of this near-optimal range are dependent on *Li*; however, as a rule of thumb the range $\psi = 0.3$–1 provides at least 80 % optimal efficiency across the full range of animals considered here. The $v_\perp^*$ profiles within these limits are shown in figure 11(*b*), where we can see that they range from a single flattened peak, to a double peak with a large central dip.

The slip ratio and Strouhal number can only provide an approximate description of tail-tip motion; however, the kinematic data required to directly extract full $v_\perp$ profiles are typically not included in published work. One exception to this is a study by van Leeuwen *et al.* (2015) on the swimming motions of larval zebrafish. Alongside their published analysis, van Leeuwen *et al.* (2015) include a full open-access dataset of steady-swimming video captures. The dataset contains kinematics for larval specimens

https://doi.org/10.1017/jfm.2018.14 Published online by Cambridge University Press

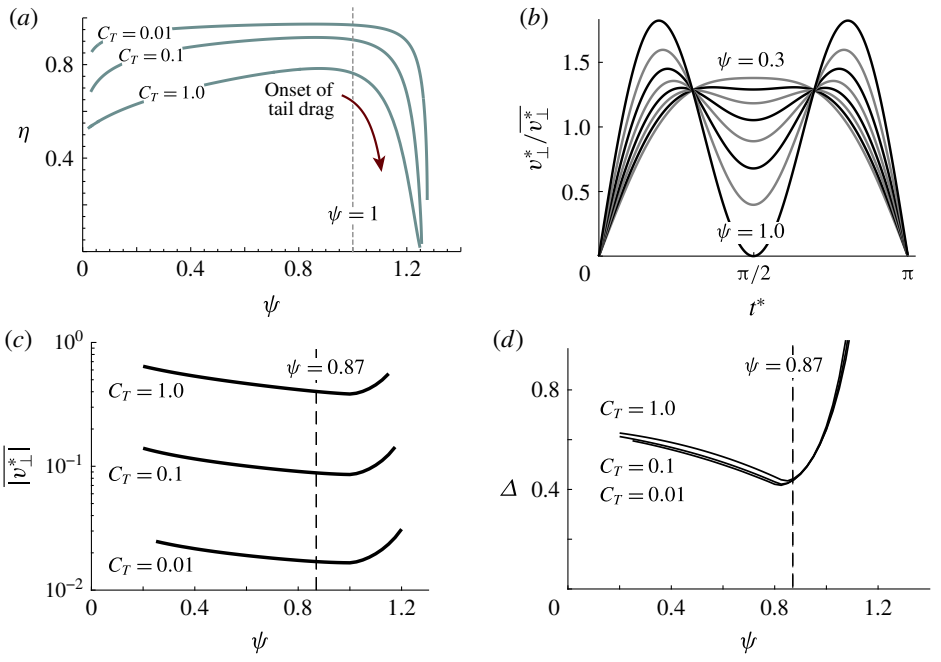


FIGURE 11. (Colour online) (*a*) Efficiency versus ψ for three different levels of thrust output. The curves exhibit a plateau in the optimal region with a sharp drop-off at the limits, $\psi = 0$ and $\psi \approx 1.27$. (*b*) $v_\perp^*$ profiles within the efficient range $\psi = 0.3$–1.0. (*c*) Average magnitude of $v_\perp^*$ plotted against ψ along constant thrust curves. (*d*) Average variation in C_T plotted against ψ along constant thrust curves; Δ is defined in (4.4).

at various stages of development, ranging from 1 to 5 days postfertilization (dpf). The swimming motions of a 5 dpf specimen are shown in figure 12(*a*), with the corresponding $v_\perp$ profile shown in figure 12(*b*). The central dip associated with optimality under Lighthill's model is clearly visible; the shape of the measured profile is well approximated by the theoretical profile at $\psi = 0.55$. In this particular case the profile is quite clear and symmetric; however, this shape can vary significantly across different swimming recordings. To address this, we consider the average profile produced by the 4 dpf and 5 dpf specimens. These groups are chosen because they consistently swam in the highest Reynolds number range ($Re \approx 10^3$) among all specimens. The dataset contains 8 unique recordings of 4 dpf specimens and 11 unique recordings of 5 dpf specimens. The mean profiles measured from each of these recordings are shown in figure 12(*c*,*d*). There is significant variation among the profiles; however, the majority of them exhibit the predicted flattened or depressed region at $t^* = \pi/2$. The average profile for all recordings within each group is shown in figure 12(*e*,*f*). The resulting curves exhibit the central plateau associated with efficient swimming and are reasonably approximated by the theoretical profile corresponding to $\psi = 0.4$. This value is close to the observed peak in the distribution of figure 10 and falls within the predicted 80 % optimal range.

5.3. *Characterizing optimal swimming behaviours*

In the case of foil-tailed swimmers, previous work has shown that *St* is strongly linked to optimality through its impact on the vortex wake (Triantafyllou *et al.* 2000).

https://doi.org/10.1017/jfm.2018.14 Published online by Cambridge University Press

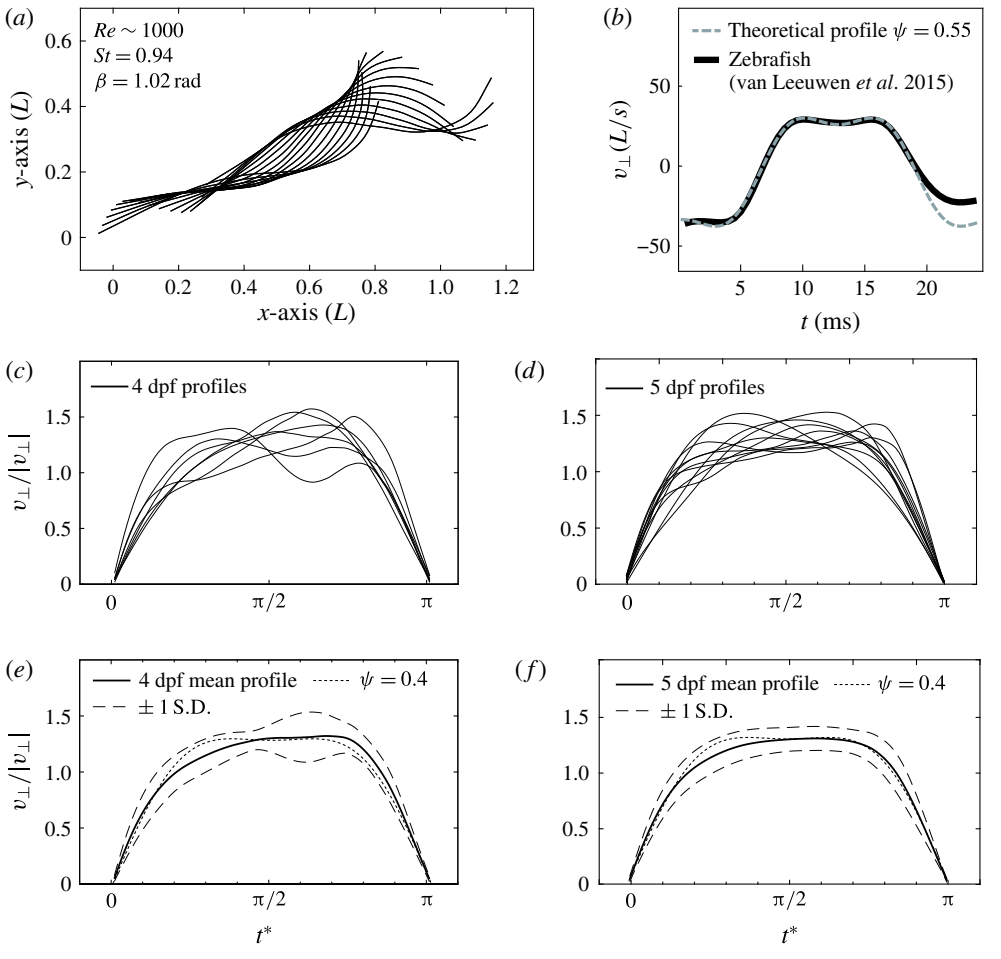


FIGURE 12. (Colour online) (*a*,*b*) Swimming motions and $v_\perp$ profile of 5 dpf zebrafish larva from open-access dataset of van Leeuwen, Voesenek & Müller (2015). Variable L corresponds to the body length of the swimmer. (*c*,*d*) Normal velocity profiles from individual recordings of 4 and 5 dpf specimens. (*e*,*f*) Mean velocity profile across all swimming recordings for 4 and 5 dpf specimens.

In contrast to this, our analysis suggests that for slender swimmers the link between optimality and St may be much weaker. Within Lighthill's model the Strouhal number of an optimal swimmer is simply determined by thrust–drag balance. As shown in figure 13(*a*), the vertical axis of our kinematic space, ψ, describes profile shape, while the horizontal axis, St, describes profile magnitude. A swimming animal which tunes its undulations to sit in the optimal ψ region will naturally settle at an appropriate St value, where the thrust output of its tail balances the drag of its body.

That being said, this does not mean that St is completely decoupled from swimming performance. As shown in figure 13(*b*), animals with body shapes and tail sizes which allow them to swim in the lower-St range are significantly more efficient than their high-St counterparts. Furthermore, figure 10 shows that the $\eta > 0.8\eta_{max}$ bounds span a much wider range when St is low; meaning that animals in this region remain reasonably efficient across a much broader range of kinematics. Within the context

https://doi.org/10.1017/jfm.2018.14 Published online by Cambridge University Press

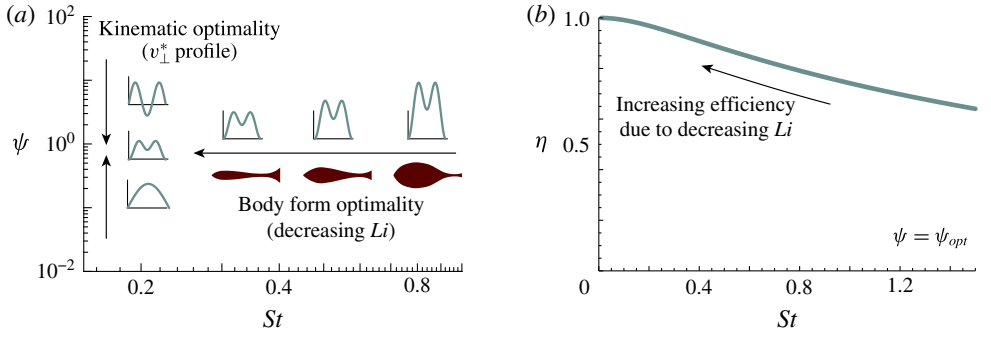


FIGURE 13. (Colour online) (*a*) ψ describes the shape of a swimming animal's $v_\perp^*$ profile, while *St* determines its magnitude. (*b*) Peak achievable efficiency is higher for animals with a tail loading, *Li*, which allows them to swim at lower *St* values.

of Lighthill's model, ψ and *St* can be thought of as characterizing the optimality of two distinct properties of a swimming animal. While ψ describes the optimality of an animal's swimming movements, *St* describes the optimality of its body form. As shown in figure 13(*a*), low *St* values indicate that an animal has a streamlined body and large tail, designed for high propulsive efficiency.

6. Conclusion

Throughout the past century researchers have sought a reductionist description of swimming motion. Beginning with Lighthill's classical small-amplitude analysis, which identified the slip ratio as the central kinematic variable, followed by breakthroughs of Triantafyllou and his collaborators on the significance of the Strouhal number. Here we have shown that, for slender animals, optimally efficient swimming kinematics can be reduced to a new parameter, ψ, defined by a function of both V/c and *St*. This new variable, ψ, characterizes how tail-tip velocity varies throughout the swimming motion. Using Lighthill's large-amplitude model, we have shown that near-optimal efficiency is achieved in the range $0.3 < \psi < 1.0$, where the average magnitude of the tail-tip velocity is minimized and the instantaneous thrust coefficient varies as little as possible throughout the swimming stroke.

This link between thrust variation and efficiency is shared by many other biological systems. A classical example is Keller's analysis of optimal running strategy for human athletes (Keller 1974). Keller shows that the best overall strategy for long races is to run at a constant velocity. This result stems from a mathematical problem structure which is similar to the one outlined here. For swimming animals, this result suggests that improved gaits could be developed by including additional harmonics in the tail motion, with the goal of reducing thrust variation. For foil-tail swimmers, Prempraneerach, Hover & Triantafyllou (2003) demonstrate that modifying kinematics to smooth the angle of attack profile can significantly improve swimming efficiency.

In terms of next steps, significant insight could be gained from an experimental study of the concepts laid out here. There is very little experimental data on the hydrodynamics of undulating elongated bodies; however, a number of parametric studies on flapping foils have produced results that resemble the thrust and efficiency maps predicted by Lighthill's model. Bandyopadhyay *et al.* (2012) study the propulsive performance of a sinusoidally flapping wing over a grid of *St* and β

https://doi.org/10.1017/jfm.2018.14 Published online by Cambridge University Press

values ranging from $St = 0.2$–1.4 and $\beta = 0.25$–1.5. They show that both parameters are required to characterize the efficiency of the foil. The resulting contours of thrust and efficiency are qualitatively similar to those of Lighthill's model, with the optimally efficient region lying along a $St - \beta$ curve which is analogous to the $St - V/c$ relationship identified here. Hover, Haugsdal & Triantafyllou (2004) conduct a parametric study of flexible foils over a similar parameter range; again the resulting contours and optimal efficiency curve are similar to those predicted by Lighthill's theory. This correspondence is somewhat surprising given the differences between the two systems. For foil-tailed swimmers, propulsive force is generated in the direct vicinity of vortex shedding. Based on this, wake effects should be critical to the swimming performance of these animals. Lighthill predicts the existence of a similar vortex wake for elongated swimmers, but his analysis takes its effects to be negligible. Since thrust is generated along the entire length of the body, he assumes that vortices shed from the tail propagate away without significantly altering the force distribution over the body surface. Any firm conclusions on the relationship between these systems will undoubtedly require further experimental or computational investigation; however, the striking predictions of Lighthill's models suggest that it captures at least some of the physical effects which motivate the behaviour of efficient slender animals.

Acknowledgements

This material is based in part upon work supported by the National Science Foundation under grant no. DMS-1517842. Any opinions, findings, and conclusions or recommendations expressed in this material are those of the author(s) and do not necessarily reflect the views of the National Science Foundation.

Supplementary materials

Supplementary materials are available at https://doi.org/10.1017/jfm.2018.14.

Appendix A. Relating tail angle and slip ratio

Within our swimming model we define the motions of the tail's trailing edge in terms of angle $\theta(t)$ and position $\boldsymbol{r}(t)$:

$$\boldsymbol{r}(t) = Vt\,\hat{\boldsymbol{e}}_x + A\cos(2\pi ft)\,\hat{\boldsymbol{e}}_y\,, \quad \text{and} \quad \theta(t) = \beta\sin(2\pi ft). \tag{A 1a,b}$$

The amplitude of the pitching motion is determined by β; however, this kinematic quantity is rarely measured in biological studies. To compare the predictions of the model to existing data we relate the pitching amplitude β to the slip ratio V/c which is more commonly recorded. This relation is derived by assuming that the body undulations of swimming animals can be approximated as a sinusoidal wave. Here, we consider two possible mathematical definitions for this wave:

$$y_1(x,t) = A(x)\cos\left(2\pi\left(ft - \frac{x}{\lambda}\right)\right), \tag{A 2}$$

$$y_2(s,t) = A(s)\cos\left(2\pi\left(ft - \frac{s}{\lambda}\right)\right). \tag{A 3}$$

In the first definition, body position is taken to be a sinusoidal function of the inertial coordinate x, while in the second it is taken to be a sinusoidal function

https://doi.org/10.1017/jfm.2018.14 Published online by Cambridge University Press

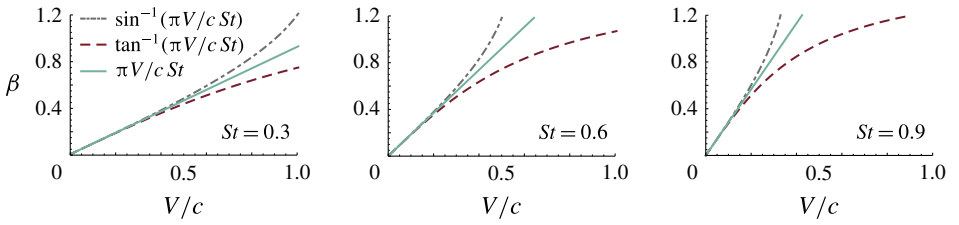


FIGURE 14. (Colour online) Comparison of alternative relations for slip ratio and pitch angle amplitude.

of the body coordinate s. Both approaches provide reasonable approximations of swimming motion; however, they yield slightly different relationships between β and V/c. To define these relationships, we first define the body angle in terms of the body wavefunctions:

$$\theta_1(x,t) = \tan^{-1}\left(\frac{\partial y_b}{\partial x}\right) \quad \text{and} \quad \theta_2(s,t) = \sin^{-1}\left(\frac{\partial y_b}{\partial s}\right), \tag{A 4a,b}$$

$$\theta_1(x,t) = \tan^{-1}\left(\frac{2\pi A(x)}{\lambda}\sin\left(2\pi\left(ft-\frac{x}{\lambda}\right)\right)+\frac{\mathrm{d}A(x)}{\mathrm{d}x}\sin\left(2\pi\left(ft-\frac{x}{\lambda}\right)\right)\right), \tag{A 5}$$

$$\theta_2(s,t) = \sin^{-1}\left(\frac{2\pi A(s)}{\lambda}\sin\left(2\pi\left(ft-\frac{s}{\lambda}\right)\right)+\frac{\mathrm{d}A(s)}{\mathrm{d}s}\sin\left(2\pi\left(ft-\frac{x}{\lambda}\right)\right)\right). \tag{A 6}$$

The amplitude derivative at the trailing edge ($s=\ell$, $x=\ell$) is assumed to be zero such that the wave is consistent with the motion defined in (A 1). β is taken to be equal to the peak value of the body angle at the tail. This yields the following relations for β and V/c:

$$\beta_1 = \arctan\left(\frac{2\pi A(\ell)}{\lambda}\right) = \arctan\left(\pi\frac{V}{c}St\right), \tag{A 7}$$

$$\beta_2 = \arcsin\left(\frac{2\pi A(\ell)}{\lambda}\right) = \arcsin\left(\pi\frac{V}{c}St\right). \tag{A 8}$$

In figure 14 the two relations are compared to one another at three different values of St. For $\pi V/cSt < 1$ the two relations are similar; however, as this term grows the two relations begin to diverge. In each plot we include a third curve representing the simplified relation, $\beta = \pi V/cSt$. Over the range of β values relevant to swimming, this simplified relation provides a compromise between the two previously presented alternatives while also being much simpler mathematically. Based on this, we apply the simplified relation for β and V/c throughout our analysis.

Appendix B. How do efficient swimmers generate thrust?

Within Lighthill's model swimming animals produce thrust through two distinct sources: the normal force ($\boldsymbol{F}_n$) and a tangential force ($\boldsymbol{F}_t$). These two terms compose the thrust coefficient within our optimization problem. In figure 15 we plot the ratio

https://doi.org/10.1017/jfm.2018.14 Published online by Cambridge University Press

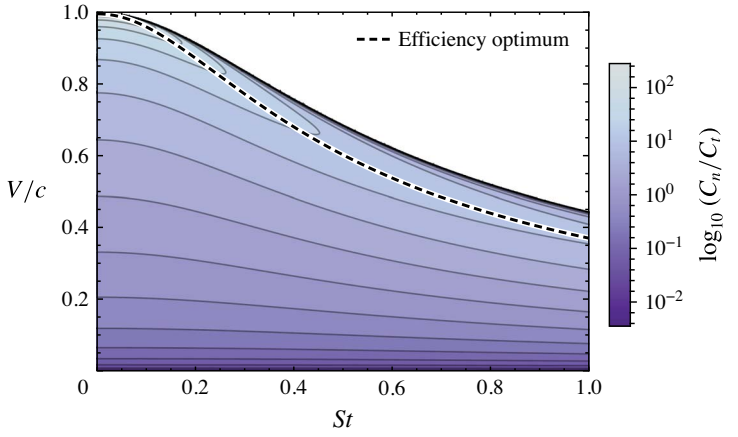


FIGURE 15. (Colour online) Ratio of thrust from the tangential and normal forces. In the optimally efficient region, the normal force is roughly 10–100 times greater than tangential force.

of the thrust components over the $St - V/c$ plane. This ratio C_n/C_t is defined as

$$\frac{C_n}{C_t} = \frac{\displaystyle\int_0^{2\pi} v_\parallel^* v_\perp^* \sin(\theta(t^*))\,\mathrm{d}t^*}{\displaystyle\int_0^{2\pi} \frac{1}{2} v_\perp^{*2} \cos(\theta(t^*))\,\mathrm{d}t^*}. \tag{B 1}$$

The contours of figure 15 illustrate how the relative contributions of the two thrust sources vary in relation to kinematics. Within the most efficient region of the map, the normal force accounts for almost all of the thrust generated by the animal. The advantage of thrust from this source can be shown by considering the thrust-to-power ratio C_T/C_P:

$$\frac{C_T}{C_P} = \frac{C_t}{C_P} + \frac{C_n}{C_P}. \tag{B 2}$$

The two terms within C_T/C_P represent the thrust-to-power ratio of each thrust source. Under the constraints $St \geqslant 0$ and $0 \leqslant \beta \leqslant \pi/2$, the upper bound of C_t/C_P is one, while the upper bound of C_n/C_P is infinity. Substituting these bounds into (2.15) reveals that thrust from the tangential force can never exceed 50 % efficiency, while thrust from the normal force can approach 100 %.

Appendix C. Lighthill's large-amplitude elongated-body theory

The notation used throughout our analysis is differs from that of Lighthill (1971). We define the average thrust produced by the swimmer as follows, where m is the hydrodynamic mass at the trailing edge:

$$\overline{T} = f \int_0^{1/f} (\boldsymbol{F}_n(t) + \boldsymbol{F}_t(t)) \cdot \hat{\boldsymbol{e}}_x \,\mathrm{d}t, \tag{C 1}$$

$$\boldsymbol{F}_n(t) = m \left(v_\parallel^* v_\perp^*\right) \hat{\boldsymbol{e}}_\perp, \tag{C 2}$$

$$\boldsymbol{F}_t(t) = m \left(\tfrac{1}{2} v_\perp^{*2}\right) \hat{\boldsymbol{e}}_\parallel, \tag{C 3}$$

https://doi.org/10.1017/jfm.2018.14 Published online by Cambridge University Press

and

$$\hat{\boldsymbol{e}}_\perp = [\sin\theta \;\; \cos\theta], \quad \hat{\boldsymbol{e}}_\parallel = [-\cos\theta \;\; \sin\theta]. \tag{C 4a,b}$$

Using equation (C 4), the thrust integral reduces to the following scalar result:

$$\overline{T} = m\int_0^{2\pi} \left(v_\parallel v_\perp \sin(\theta) + \frac{1}{2} v_\perp^2 \cos(\theta) \right) \mathrm{d}t. \tag{C 5}$$

Within Lighthill's derivation $v_\parallel$ and $v_\perp$ are denoted by the variables u and w and the projections $\cos\theta$ and $\sin\theta$ are given by the spatial derivatives $\partial x/\partial a$ and $\partial z/\partial a$, where x is equivalent to our x coordinate, z is equivalent to our y coordinate, and a is a curvilinear coordinate along the swimmer's spine. Making these substitutions we see that equation (C 5) is equivalent to the time average of the horizontal thrust component of equation (5) in Lighthill (1971):

$$\overline{T} = m\int_0^{2\pi} \left(uw\frac{\partial z}{\partial a} + \frac{1}{2} w^2 \frac{\partial x}{\partial a} \right) \mathrm{d}t. \tag{C 6}$$

Equation (7) of Lighthill (1971) reduces this to the more compact form

$$\overline{T} = m\int_0^{2\pi} w \left(\frac{\mathrm{d}z}{\mathrm{d}t} - \frac{1}{2} w \frac{\partial x}{\partial a} \right) \mathrm{d}t. \tag{C 7}$$

The details of the reduction process are not included in Lighthill (1971); we provide them here to demonstrate the equivalence of the two forms. Starting with (C 5), we begin by separating $(1/2)v_\perp^2 \cos\theta$ into two terms and factoring out $v_\perp$:

$$\overline{T} = m\int_0^{2\pi} v_\perp \left(v_\parallel \sin(\theta) + v_\perp \cos(\theta) - \frac{1}{2} v_\perp \cos(\theta) \right) \mathrm{d}t. \tag{C 8}$$

The velocity terms in (C 8) can be expanded as follows:

$$v_\perp = \frac{\mathrm{d}\boldsymbol{r}}{\mathrm{d}t} \cdot \hat{\boldsymbol{e}}_\perp, \quad v_\parallel = \frac{\mathrm{d}\boldsymbol{r}}{\mathrm{d}t} \cdot \hat{\boldsymbol{e}}_\parallel, \tag{C 9a,b}$$

$$v_\perp = \frac{\mathrm{d}x}{\mathrm{d}t}\sin\theta + \frac{\mathrm{d}y}{\mathrm{d}t}\cos\theta, \quad v_\parallel = -\frac{\mathrm{d}x}{\mathrm{d}t}\cos\theta + \frac{\mathrm{d}y}{\mathrm{d}t}\sin\theta. \tag{C 10a,b}$$

Substituting these expressions into (C 8) produces the following result:

$$\overline{T} = m\int_0^{2\pi} v_\perp \left(-\frac{\mathrm{d}x}{\mathrm{d}t}\cos\theta\sin\theta + \frac{\mathrm{d}y}{\mathrm{d}t}\sin^2\theta + \frac{\mathrm{d}x}{\mathrm{d}t}\sin\theta\cos\theta + \frac{\mathrm{d}y}{\mathrm{d}t}\cos^2\theta - \frac{1}{2}v_\perp\cos(\theta) \right) \mathrm{d}t, \tag{C 11}$$

which then collapses to

$$\overline{T} = m\int_0^{2\pi} v_\perp \left(\frac{\mathrm{d}y}{\mathrm{d}t} - \frac{1}{2} v_\perp \cos(\theta) \right) \mathrm{d}t. \tag{C 12}$$

Converting this result to Lighthill's notation we see that it is equivalent to equation (7) of Lighthill (1971):

$$\overline{T} = m\int_0^{2\pi} w \left(\frac{\mathrm{d}z}{\mathrm{d}t} - \frac{1}{2} w \frac{\partial x}{\partial a} \right) \mathrm{d}t. \tag{C 13}$$

https://doi.org/10.1017/jfm.2018.14 Published online by Cambridge University Press

REFERENCES

BAINBRIDGE, R. 1958 The speed of swimming of fish as related to size and to the frequency and amplitude of the tail beat. *J. Expl Biol.* **35** (1), 109–133.

BANDYOPADHYAY, P. R., BEAL, D. N., HRUBES, J. D. & MANGALAM, A. 2012 Relationship of roll and pitch oscillations in a fin flapping at transitional to high Reynolds numbers. *J. Fluid Mech.* **702**, 298–331.

BLAKE, R., LI, J. & CHAN, K. 2009 Swimming in four goldfish *Carassius auratus* morphotypes: understanding functional design and performance employing artificially selected forms. *J. Fish Biol.* **75** (3), 591–617.

CLARK, R. P. & SMITS, A. J. 2006 Thrust production and wake structure of a batoid-inspired oscillating fin. *J. Fluid Mech.* **562**, 415–429.

DABIRI, J. O. 2009 Optimal vortex formation as a unifying principle in biological propulsion. *Annu. Rev. Fluid Mech.* **41** (1), 17–33.

ELOY, C. 2012 Optimal Strouhal number for swimming animals. *J. Fluids Struct.* **30**, 205–218.

ELOY, C. 2013 On the best design for undulatory swimming. *J. Fluid Mech.* **717**, 48–89.

GAZZOLA, M., ARGENTINA, M. & MAHADEVAN, L. 2014 Scaling macroscopic aquatic locomotion. *Nat. Phys.* **10** (10), 758–761.

GRAY, J. 1936 Studies in animal locomotion: VI. The propulsive powers of the dolphin. *J. Expl Biol.* **13** (2), 192–199.

HOVER, F. S., HAUGSDAL, O. & TRIANTAFYLLOU, M. S. 2004 Effect of angle of attack profiles in flapping foil propulsion. *J. Fluids Struct.* **19** (1), 37–47.

JAYNE, B. C. & LAUDER, G. V. 1995 Speed effects on midline kinematics during steady undulatory swimming of largemouth bass, *Micropterus salmoides*. *J. Expl Biol.* **198** (2), 585–602.

KELLER, J. B. 1974 Optimal velocity in a race. *Am. Math. Mon.* **81** (5), 474–480.

KERN, S. & KOUMOUTSAKOS, P. 2006 Simulations of optimized anguilliform swimming. *J. Expl Biol.* **209** (24), 4841–4857.

LANGERHANS, R. B. 2009 Trade-off between steady and unsteady swimming underlies predator-driven divergence in *Gambusia affinis*. *J. Evol. Biol.* **22** (5), 1057–1075.

VAN LEEUWEN, J. L., VOESENEK, J. & MÜLLER, U. K. 2015 How body torque and Strouhal number change with swimming speed and developmental stage in larval zebrafish. *J. R. Soc. Interface* **12** (110), 20150479.

LIAO, J. C. 2002 Swimming in needlefish (Belonidae): anguilliform locomotion with fins. *J. Expl Biol.* **205** (18), 2875–2884.

LIGHTHILL, M. J. 1960 Note on the swimming of slender fish. *J. Fluid Mech.* **9** (2), 305–317.

LIGHTHILL, M. J. 1969 Hydromechanics of aquatic animal propulsion. *Annu. Rev. Fluid Mech.* **1**, 413–446.

LIGHTHILL, M. J. 1971 Large-amplitude elongated-body theory of fish locomotion. *Proc. R. Soc. Lond.* B **179** (1055), 125–138.

LIGHTHILL, S. 1975 *Mathematical Biofluiddynamics*. Society for Industrial and Applied Mathematics.

LINDEN, P. F. & TURNER, J. S. 2001 The formation of optimal vortex rings, and the efficiency of propulsion devices. *J. Fluid Mech.* **427**, 61–72.

LINDEN, P. F. & TURNER, J. S. 2004 Optimal vortex rings and aquatic propulsion mechanisms. *Proc. R. Soc.* **271** (1539), 647–653.

LONG, J., HALE, M., MCHENRY, M. & WESTNEAT, M. 1996 Functions of fish skin: flexural stiffness and steady swimming of longnose gar, *Lepisosteus osseus*. *J. Expl Biol.* **199** (10), 2139–2151.

MAERTENS, A. P., GAO, A. & TRIANTAFYLLOU, M. 2017 Optimal undulatory swimming for a single fish-like body and for a pair of interacting swimmers. *J. Fluid Mech.* **813**, 301–345.

VON MISES, L. 1959 *Theory of Flight*. Dover Publications.

MOORED, K. W., DEWEY, P. A., BOSCHITSCH, B. M., SMITS, A. J. & HAJ-HARIRI, H. 2014 Linear instability mechanisms leading to optimally efficient locomotion with flexible propulsors. *Phys. Fluids* **26** (4), 041905.

MOORED, K. W., DEWEY, P. A., SMITS, A. J. & HAJ-HARIRI, H. 2012 Hydrodynamic wake resonance as an underlying principle of efficient unsteady propulsion. *J. Fluid Mech.* **708**, 329–348.

https://doi.org/10.1017/jfm.2018.14 Published online by Cambridge University Press

MULLER, U. K., SMIT, J., STAMHUIS, E. J. & VIDELER, J. J. 2001 How the body contributes to the wake in undulatory fish swimming. *J. Expl Biol.* **204** (16), 2751–2762.

PREMPRANEERACH, P., HOVER, F. S. & TRIANTAFYLLOU, M. S. 2003 The effect of chordwise flexibility on the thrust and efficiency of a flapping foil. In *UUST 03: 13th International Symposium on Unmanned Untethered Submersible Technology*, pp. 1–10.

RASPA, V., RAMANANARIVO, S., THIRIA, B. & GODOY-DIANA, R. 2014 Vortex-induced drag and the role of aspect ratio in undulatory swimmers. *Phys. Fluids* **26** (4), 041701.

VAN REES, W., GAZZOLA, M. & KOUMOUTSAKOS, P. 2013 Optimal shapes for anguilliform swimmers at intermediate Reynolds numbers. *J. Fluid Mech.* **722**, R3.

VAN REES, W., GAZZOLA, M. & KOUMOUTSAKOS, P. 2015 Optimal morphokinematics for undulatory swimmers at intermediate Reynolds numbers. *J. Fluid Mech.* **775**, 178–188.

ROHR, J. J. 2004 Strouhal numbers and optimization of swimming by odontocete cetaceans. *J. Expl Biol.* **207** (10), 1633–1642.

TAYLOR, G. 1952 Analysis of the swimming of long and narrow animals. *Proc. R. Soc Lond.* A **214** (1117), 158–183.

TAYLOR, G. K., NUDDS, R. L. & THOMAS, A. L. R. 2003 Flying and swimming animals cruise at a Strouhal number tuned for high power efficiency. *Nature* **425** (6959), 707–711.

TOKIĆ, G. & YUE, D. K. P. 2012 Optimal shape and motion of undulatory swimming organisms. *Proc. Biol. Sci.* **279** (1740), 3065–3074.

TRIANTAFYLLOU, G. S., TRIANTAFYLLOU, M. S. & GROSENBAUGH, M. 1993 Optimal thrust development in oscillating foils with application to fish propulsion. *J. Fluids Struct.* **7** (2), 205–224.

TRIANTAFYLLOU, M. S., TRIANTAFYLLOU, G. S. & GOPALKRISHNAN, R. 1991 Wake mechanics for thrust generation in oscillating foils. *Phys. Fluids* **3** (12), 2835.

TRIANTAFYLLOU, M. S., TRIANTAFYLLOU, G. S. & YUE, D. K. P. 2000 Hydrodynamics of fishlike swimming. *Annu. Rev. Fluid Mech.* **32** (1), 33–53.

TYTELL, E. D., BORAZJANI, I., SOTIROPOULOS, F., BAKER, T. V., ANDERSON, E. J. & LAUDER, G. V. 2010 Disentangling the functional roles of morphology and motion in the swimming of fish. *Integr. Compar. Biol.* **50** (6), 1140–1154.

VIDELER, J. J. 1993 *Fish Swimming*. Chapman & Hall.

VIDELER, J. J. & HESS, F. 1984 Fast continuous swimming of two pelagic predators, saithe (*Pollachius virens*) and mackerel (*Scomber scombrus*): a kinematic analysis. *J. Expl Biol.* **109** (1), 209–228.

VIDELER, J. J. & WARDLE, C. S. 1978 New kinematic data from high-speed cine film recordings of swimming cod (*Gadus morhua*). *Netherlands J. Zool.* **28** (3-4), 465–484.

WEBB, P. W. 1986 Kinematics of lake sturgeon, *Acipenser fulvescens*, at cruising speeds. *Can. J. Zool.* **64** (10), 2137–2141.

WEBB, P. W. & KEYES, R. S. 1982 Swimming kinematics of sharks. *Fishery Bull.* **80** (4), 803–812.

WEBB, P. W., KOSTECKI, P. T. & STEVENS, E. D. 1984 The effect of size and swimming speed on locomotor kinematics of rainbow trout. *J. Expl Biol.* **109** (1), 77–95.

VAN WEERDEN, J. F., REID, D. P. & HEMELRIJK, C. K. 2014 A meta-analysis of steady undulatory swimming. *Fish Fisheries* **15** (3), 397–409.

WU, T. Y. 1971 Hydromechanics of swimming propulsion. Part 3. Swimming and optimum movements of slender fish with side fins. *J. Fluid Mech.* **46** (3), 545–568.

https://doi.org/10.1017/jfm.2018.14 Published online by Cambridge University Press